J Exp Biol Advance Online Articles. First posted online on 5 December 2013 as doi:10.1242/jeb.092940
Access the most recent version at http://jeb.biologists.org/lookup/doi/10.1242/jeb.092940

The effects of naris occlusion on mouse nasal turbinate development.

David M. Coppola[1] and Brent A. Craven[2]

[1]Department of Biology, Randolph-Macon College, Ashland, VA, USA. [2]Department of Mechanical and Nuclear Engineering, Gas Dynamics Laboratory, Pennsylvania State University, PA, USA

Short Title: Effect of naris occlusion on nasal turbinates

Keywords: airflow, nasal development, airway remodeling

Corresponding Author:

David Coppola

Department of Biology

Randolph Macon College

304 Caroline St

Ashland, VA 23005 USA

Phone: 804-752-3147

Fax: 804-752-4724

Email: dcoppola@rmc.edu

SUMMARY

Unilateral naris occlusion, a standard method for causing odor deprivation, also alters airflow on both sides of the nasal cavity. We reasoned that manipulating airflow by occlusion could affect nasal turbinate development given the ubiquitous role of environmental stimuli in ontogenesis. To test this hypothesis, newborn mice received unilateral occlusion or sham surgery and were allowed to reach adulthood. Morphological measurements were then made of paraffin sections sampled throughout the nasal cavity. Occlusion significant affected the size, shape, and position of turbinates. In particular, the nasoturbinate, the focus of our quantitative analysis, had a more delicate appearance on the occluded side relative to the open side. Occlusion also caused an increase in the width of the dorsal meatus within the non-occluded and occluded nasal fossae, compared to controls, and the position of most turbinates was altered. These results suggest that a mechanical stimulus from respiratory airflow is necessary for the normal morphological development of turbinates. To explore this idea, we estimated the mechanical forces on turbinates due to airflow during normal respiration that would be abrogated by occlusion. MRI scans were used to construct a 3D model of the mouse nasal cavity that provided the input for a computational fluid dynamics simulation of nasal airflow. The simulation revealed maximum shear stress values for the walls of turbinates in the 1 Pa range, a magnitude that causes remodeling in other biological tissues. These observations raise the intriguing possibility that nasal turbinates develop partly under the control of respiratory mechanical forces.

INTRODUCTION

Perhaps the least-known identifying characteristic of the class Mammalia is the possession of highly intricate epithelium-covered bony-plates within the nasal cavity collectively known as turbinates (Negus, 1958). Each nasal fossa contains three sets of these bilateral structures: maxilloturbinates, nasoturbinates, and ethmoturbinates, named for their skull-bone of attachment (Rowe et al., 2005). Turbinates, through their branching and scrolling geometry, greatly increase the surface area of the overlying mucosal epithelium and thus increase its ability to exchange with the environment. These adaptations for increased exchange promote two quintessentially mammalian characteristics: endothermy and an exceptional reliance on olfaction for survival. Maxilloturbinates and nasoturbinates, lying rostrally in the nasal fossae and covered largely with respiratory epithelium, heat and moisturize inspired air while reclaiming heat and moisture from exhaled air (Moore, 1981). These "respiratory" turbinates are especially pronounced in aquatic species for which heat loss is a constant threat (Van Valkenburgh et al., 2011). In contrast, ethmoturbinates are most fully elaborated in macrosmatic species such as canids and rodents (Moore, 1981). These labyrinthian plates, lying dorsocaudally in the nasal fossae, are covered with a combination of respiratory (non-sensory) and olfactory (sensory) epithelium (Negus, 1958) and are mostly protected within blind-recesses outside the main respiratory airstream (Craven et al., 2007).

Turbinates remain among the least studied parts of the mammalian skull despite the fact that they are hallmarks of the class and comprise a large portion of the skull's volume (Rowe, et al., 2005). While a smattering of descriptive studies, dating back to at least the 19th century (eg. Allen, 1882), have been reported, surprisingly little is known about turbinate ontogeny and functional morphology. The basic plan of the nasal cavity and turbinates seems to be conserved among most terrestrial mammals (Moore, 1981). While, differences in the size, shape and number of turbinates exist across even closely related species, the functional significance of these differences remains poorly understood (Van Valkenburgh et al., 2004). Turbinates originate from the embryonic olfactory capsule then increase in size and complexity during an extended postnatal development (Rowe et al., 2005). Data are lacking on the developmental mechanisms governing the formation of the complex morphology of turbinates including the positioning of their interlocking plates, scrolls, and arbors that maximize surface area for exchange while minimizing air resistance.

This study focuses on mechanical factors that might influence the ontogenesis of turbinates. It was reasoned that, since turbinates emerge largely postnatally (Ginn et al., 2008), respiratory airflow might play an instructive role in their growth and positioning. In order to test this hypothesis we examined the effects of unilateral naris occlusion (UNO) on turbinate development (Gudden, 1870; Meisami, 1976). UNO is a standard method for producing odor deprivation in studies of sensory plasticity that has profound effects on the developing olfactory system (reviewed by Coppola, 2012). However, this manipulation also causes marked airflow changes in both the occluded and non-occluded (open) nasal fossae. While on the occluded side the airflow is dramatically reduced, especially rostral to the septal window (rostral extension of the nasopharyngeal meatus along the midline), the open side is forced to carry a larger-than-normal volume of air. Also, UNO abrogates alternating cycles of breathing, forcing constant duty on the open side. Thus, if airflow affects turbinate development, one would expected to see differences in morphology among the turbinates from occluded, open, and control nasal fossae. The results of this study confirm that turbinate morphology in the open and occluded fossae of UNO mice is differentially affected compared with controls, suggesting a role for respiratory airflow in normal turbinate ontogeny. Moreover, our numerical simulation of mouse respiration confirms that shear forces on the turbinate walls reach levels sufficient to induced tissue remodeling.

RESULTS

Turbinate morphology in normal animals was noteworthy for its remarkable bilateral symmetry (Fig. 1A). In contrast, a marked asymmetry of turbinates was apparent in the occluded compared to the open nasal fossa of UNO subjects. This difference was most obvious in the rostrally located Nt and Mt. These structures appeared shorter and more robust in the open nasal fossa than in the occluded fossa, the latter taking on a filigree-like appearance (Fig. 1B and D). This effect was observed throughout the rostrocaudal extent of these rostral turbinates (Fig. 1E).

Quantification of the UNO effect focused on Nt (see Materials and Methods). Consistent with our observations, the cross-sectional area of Nt was greater in the open nasal fossa than in the occluded fossa. This difference was apparent at all rostrocaudal-sampling locations and in both age groups (Fig. 2A & C.) exceeding 70% in some cases. In contrast, the perimeter of Nt was virtually identical at any given rostrocaudal location when the occluded and open fossa were

compared. Measurements of Nt area and perimeter from normal animals (Fig. 2B & D) confirmed our visual impression of remarkable bilateral symmetry. For statistical purposes, the average ratio of Nt area to perimeter (A/P) was determined for each subject and the group means were compared (Fig. 2E). As predicted from an examination of the individual profiles, A/P values of Nt from the open nasal fossa were significantly greater than those from the occluded side ($t = 4.58$, $df = 6$, two-tailed $p < 0.004$). That this effect was not simply due to a diminution of Nt on the occluded side was born out by comparisons to control subjects. The A/P values of Nt from controls was significantly *less* than those from open nasal fossae ($t = 1.92$, $df = 7$ corrected, one-tailed $p < 0.05$) and significantly *greater* than those from occluded nasal fossae ($t = 4.57$, $df = 8$ corrected, one-tailed $p < 0.001$).

Measurements of Nt length and width were obtained to further characterize the effect of UNO on turbinate morphology. Nt tended to be slightly longer and much thinner on the occluded side at most rostrocaudal locations for both ages (Fig. 3A & C). This difference contrasts with the high degree of bilateral symmetry in length and width measurements from control subjects (Fig. 3B & D). With regard to the group data, the average ratio of Nt length to width (L/W) was significantly greater for occluded fossae than for the open fossae ($t = 7.0$, $df = 6$, two-tailed $p < 0.0004$) consistent with the former's filigree appearance (Fig. 3E). As was the case for A/P ratio, the L/W ratio for normal Nt was intermediate between the values for open and occluded fossae, however, the latter means were not significantly different ($t = 0.7$, $df = 8$ corrected, one-tailed $p > 0.05$). Length of Nt, considered separately, averaged 7.6 % longer on the occluded side than in open-side counterparts, a difference that was statistically significant ($t = 4.1$, $df = 6$, $p < 0.002$).

The effects of UNO on the nasal fossae were not limited to turbinate dimensions. The maximum mediolateral extent of the dorsal meatus (W) was greater in the occluded fossae than the open fossae, an effect that was more obvious rostrally (Fig. 4A & C). This measurement in normal animals was marked by the same bilateral symmetry as A/P values and L/W values (Fig. 4B & D). In contrast to those measurements, however, where normal subjects tended to be intermediate between occluded and open, normal subjects tended to have the smallest W values. With regard to the group data, occluded fossae had significantly larger W values than open fossae ($t = 2.9$, $df = 7$, two-tailed $p < 0.02$) or normal fossae ($t = 4.9$, $df = 8$ corrected, one-tailed p

< 0.0006) while open fossae had larger W values than normal fossae (t = 3.3, df = 9 corrected, one-tailed $p < 0.005$; Fig. 4E).

UNO also had an effect on turbinate position. To quantify this effect, a turbinate's displacement (offset) from its nearest point to the septum was measured at intervals along its rostrocaudal extent. Average turbinate-septum offsets were greatest for occluded fossae compared to open or normal fossae (Fig. 5A-C). Indeed, the difference between occluded fossae and open fossae only failed to reach statistical significance for endoturbinate II_{dorsal} (paired t-test, two-tailed $p > 0.05$) though even this turbinate's direction and magnitude of mean differences were similar to the results for the others. However, for endoturbinate-IV the average magnitude of the difference between occluded-side offsets and open-side offsets was small and the former did not differ statistically from values for normal fossae (unpaired t-test, one-tailed $p < 0.05$ criterion). Offsets for turbinates from open fossae tended to be similar to those from normal fossae except in the case of Nt where open-side offsets were statistically greater than for normal turbinates (unpaired t-test, one-tailed $p < 0.05$ criterion; Fig. 5C).

The distribution of shear stress magnitudes in the right nasal fossa of a normal adult mouse derived from our Computational Fluid Dynamics (CFD) simulations is shown in Fig. 6. The contours of shear stress on cross-sections of the airway wall, shown as insets (1-4 respiratory region and 5, 6 olfactory region) are particularly noteworthy. Maximum estimated shear stresses on the walls of Nt and Mt exceeds 1 Pa at some loci in the most rostral cross-sections decreasing caudally. In the olfactory region, maximum shear stress is as much as two orders of magnitude lesser in the range of 0.01 - 0.1 Pa. Thus, in general, shear stress declines along the walls of the nasal cavity from a maximum at the external naris to its lowest levels moving dorsally and caudally in the nasal fossa.

DISCUSSION

To our knowledge this is the first study to examine the effects of respiratory airflow on the development of nasal turbinates and airspaces. Manipulating airflow by UNO influenced the size, shape, and position of turbinates as well as the size of fossae in the nasal capsule. Turbinates in the occluded nasal fossa, where airflow would be much reduced following UNO, took on a fine filigree-like appearance with somewhat longer and substantially thinner

dimensions. The opposite effect occurred in the open nasal fossa where airflows would be greater than normal following UNO. Compared to controls, turbinates in the open nasal fossa were somewhat shorter and substantially thicker. This effect was only quantified for Nt but was apparent in other turbinates, though its magnitude decreased caudally. In addition, UNO caused turbinates in both the occluded and open nasal fossae to shift laterally in position, an effect which was most pronounced rostrally and dorsally. Finally, UNO caused a widening of the dorsal meatus, the dorsal-most airway of the nasal cavity, on both the occluded and open nasal fossae compared to controls. This effect was significantly more pronounced on the occluded side.

A likely cause of the differences, described above, among the open, occluded and normal turbinates is the abrogation of airflow-created mechanical forces, such as wall shear stress, in the occluded nasal fossa and the enhancement of those forces in the open nasal fossa of UNO animals. Why should alterations of shear stress and perhaps other mechanical forces in the developing nasal cavity have the reported effects on nasal turbinates and fossae? We posit that that the answer lies in what has been called the "mechanostat" theory: tissues under mechanical stress grow in ways to resist such stress (Rausch, 2005). This phenomenon has been thoroughly studied in bone where increases in mechanical load trigger bone formation and inhibit bone resorption (Harada and Rodan, 2003). Conversely, bone loss accompanies decreases in mechanical load caused by immobilization due to injury or the microgravity conditions of space flight (Bass et al., 2005). While the details of this mechanism remain to be elucidated, mediators include stress-sensitive calcium channels, integrins and a host of paracrine signals including prostaglandins and nitric oxide (Harad and Rodan, 2003; Bidwell and Pavalko, 2010). The mechanical forces on most bones are created by the postural and motor actions of their attached muscles. The influence of muscle action on bone growth is exemplified by the bone asymmetry observed in athletes who participate in unilateral sports like tennis (Bass et al., 2005).

The effects of UNO shown here seem to involve both soft tissues and bone, though this was not studied in detail (data not shown). Nasal turbinates contain rather unusual bones in that they do not serve as points of origin or insertion for muscles. However, in this case respiratory airflow places time-varying mechanical loads on the turbinate bone and overlying tissue. Thus, the greater volume and constancy of airflow in the open fossa could lead to more robust tissue

growth while the reduced airflow of the occluded side could lead to dystrophy under a mechanostat regime. Similar increased robustness of nasal turbinates has been reported in brachycephalic dogs (Walter, 2010), where nasal volume is reduced and thus airflow and resistance is increased (Hueber, 2009; Lippert et al., 2010).

Our estimates of maximum shear stress for normal adult mice, in excess of 1 Pa at some rostral loci, are in line with estimates from model human nasal cavities during quiet breathing (Elad et al., 2006). This magnitude of shear stress is similar to that experienced by the walls of large arteries (Ku, 1997) and has been shown to be sufficient to influence intracellular calcium levels, cell proliferation, cytoskeletal configuration, and various cellular secretions in cultured endothelial cells (reviewed by Huang et al., 2004). Wall shear stresses in the 1Pa range, created by strain-induced fluid flow in the interstitial spaces around osteocytes, are thought to underlie bones response to loading (Ehrlich and Lanyon, 2002). Finally, wall shear stresse as low as 0.5 Pa causes increased mucin secretion in cultured nasal epithelium (Davidovich et al., 2011). Taken together, these results support our hypothesis that differences in wall shear stress in the open and occluded nasal fossa of UNO mice contribute to the reported differences in turbinate morphology, though other mechanical factors such as compressive force may also play a role. Further support for our hypothesis accrues from the fact that the more rostral Nt and Mt which are subjected to the greatest shear stress, according to the CFD simulation, evinced the greatest morphological effects.

It is important to consider whether the effects of UNO reported here might be a function of something other than airflow. Naris occlusion, performed using our method, leaves only a small area of scar tissue around the site of the original naris opening. Indeed, the wound created by the procedure is healed within a couple of days and damage to even the most rostral nasal structures is virtually undetectable. In addition, effects like those reported here are not in evidence in our archival data that included sham cautery in the vicinity of the nares (data not shown). Thus, it seems highly doubtful that the superficial skin wound and scar formation caused by UNO could produce the alterations in turbinates and fossae reported here. But, the most convincing evidence that the current results are due to airflow manipulation come from a consideration of the measurements of turbinate morphology in the control subjects. For both the A/P and L/W measurements, turbinates from control mice had an intermediate morphology

between the more robust form in the open fossa and the more filigree form in the occluded fossa. This result is inconsistent with a local effect of the UNO surgical manipulation on turbinate development. However, temperature and humidity, likely differed between the open and occluded fossa of UNO mice and these potential contributors to the reported morphological effects cannot be so easily dismissed. Indeed, mucin secretions in cultured nasal epithelium are influenced by both temperature and humidity independent of wall shear stress (Davidovich et al., 2011).

It is noteworthy that while turbinates from the occluded fossa were thinner they were also longer than turbinates from the open or normal fossa. This resulted in virtually identical perimeter (surface area) measurements between the open and occluded sides despite the difference in cross-sectional area. Perhaps this symmetry was a mere by-produce of mechanical stress differences between the open and occluded fossae. With regard to weight bearing bones, growth in length and width have opposite effects on bone strength (Rauch 2005). Lengthening increases lever arms and bending moments creating greater bone loads (Bass et al., 2005). Thus, the greater mechanical force on turbinates from the open fossa might suppress growth in length. More speculatively, perhaps the opposite effects of UNO on length and width indicate that growth of turbinates is controlled in part by the requirements for heat and moisture exchange with inspired air.

The explanation for the effects of UNO on turbinate position and dorsal meatus diameter is less obvious. One might speculate that in the open nasal fossa of UNO subjects turbinate lateral shift and dorsal meatus widening are compensatory mechanism to decrease air resistance in an overtaxed airway. However, absent further *post hoc* speculation this leaves unexplained why the occluded fossa showed the greatest turbinate lateral shift and dorsal meatus widening. Nevertheless, these effects of UNO on turbinate position and airway dimensions further establish the role of airflow in normal nasal development.

Like other organs, the eye has the ability to control its growth. Emmetropization is the term most commonly associated with this remarkable homeostatic mechanism that uses visual input to provide the necessary error signals for eye growth to self-adjust. Thus, chronically defocusing the eye of experimental animals by lens-rearing leads to rapid correction of focal distance by the appropriate modulation of ocular elongation and choroidal thickening (Wallman and Winawer, 2004). In contrast, the factors that guide the formation of the complex

morphology and remarkable symmetry of the nasal turbinates are largely unknown. The results of the current study raise the interesting possibility that nasal cavity development is substantially a product of environmental instruction, as for the eye. While a case has been made for mechanical forces of respiratory airflow being a determinant of turbinate morphology, thermal or chemical stimuli may also be influential.

Based on the current study, UNO, long used as a method of olfactory deprivation in neural plasticity research (Coppola, 2012), also presents itself as a model of brachycephalic airway syndrome in canines and nasal obstruction disorders in humans (Wu et al., 2012). The effects of UNO on the nasal capsule and its contents have obvious implications for the physiological function of these structures including their critical role in olfaction. For example, it has recently been argued that the pattern of nasal airflow created by the turbinate system is critical to the high degree of olfactory capability in macrosmatic organisms (Craven et al. 2007). In light of this hypothesis and the current findings, it is interesting that the olfactory sensory neurons, in addition to responding to odor ligands, are exquisite mechanoreceptors (Grosmaitre et al, 2007). Indeed, some of the reported effects of UNO on the olfactory system may turn out to be secondary to its effects on nasal morphology. Further research will be necessary to disentangle the effects of mechanical, thermal, and chemical stimuli on turbinate ontogenesis.

MATERIALS AND METHODS

This study is based on archival tissue sections used for the studies described in Waguespack et al. (2005) and Coppola et al. (2006). Microscopy and data analysis were performed in Leipzig Germany, Ashland, VA, USA and Boston, MA, USA. The MRI scanning and computational fluid dynamics simulation were performed in State College, PA, USA.

Animals

Animal care and experimental procedures on CD-1 strain mice (Charles River Labs Wilmington, MA, USA) followed the *Guide to the Care and Use of Laboratory Animals* (National Institutes of Health, USA) and were approved by the Randolph-Macon College and Centenary College Institutional Animal Care and Use Committees.

Naris occlusion

On the first postnatal day (PND 1), a group of anesthetized (ketamine and hypothermia) mice had either the left or right naris occluded by cauterization. Occluded mice were removed from the study if their cauterized naris was found to be patent during daily inspections. Eight mice meeting the permanent occlusion criterion formed the UNO group. Four additional mice that were untreated served as controls.

Histology

Six mice (four UNOs and two controls) at PND 18 and six mice (four UNOs and two controls) at PND 25 were deeply anesthetized (Nembutal), exsanguinated by perfusion (0.1M PBS, pH 7.2), and fixed by perfusion with Bouin's fluid. Trimmed heads were postfixed for two hours by emersion in Bouin's fluid, and dehydrated in a graded series of ethanol solutions. Heads were then cleared in Histosol, (National Diagnostics, Atlanta, GA), embedded in paraffin, and cut at 10 μm in the coronal plane. Selected groups of serial sections, collected at 50 μm intervals, were mounted on subbed microscope slides. Alternate slides were either left unstained, stained with Hematoxylin and Eosin (H&E), or were immunolabeled for OMP. In the latter case, sections were reacted for 24 hrs at 4°C with goat anti-OMP (1:30,000; gift of Frank Margolis). Immunoreactivity was visualized using an ABC kit matched to the source of the primary antibody (Vector Labs, Burlingame, CA) and DAB kit (Vector Labs). Primary antibody was omitted in some assays to establish specificity of labeling (data not shown).

Morphometrics

Microscopic inspection of prepared slides revealed an obvious effect on occluded-side nasal turbinates that was more pronounced rostrally. These turbinates took on a delicate "filigree" appearance characterised by thinning and elongation. To quantify this effect for statistical purposes, we focused on Nt, structures covered by regions of both olfactory and respiratory epithelium (Fig. 7A & B). Measurements including: cross-sectional area, perimeter, length, and width were made with the aid of the analySIS 2.1, SIS GmbH, Soft-Imaging Software (GmbH, Münster, Germany) from digital pictures (100x magnification) taken with a Sony Camera Color Video camera, CCD-Iris, 3CCD attached to an Axioskop Zeiss Microscope (Fig. 7B). Since turbinates emerge from bones of the skull, the proximal limit of Nt could not be defined unambiguously. However, care was taken to terminate the measurement of Nt as symmetrically

as possible comparing the left and right nasal fossae. For the area measurement, a cord was included in the perimeter measurement that connected the proximal termini of each turbinate's surface tracing (Fig. 7B).

Two additional measurements were made: (1) the lateral offset of each of the four ethmoturbinates from the nasal septum measured at their widest expanse and (2) the width of the dorsal meatus at its widest expanse (Fig. 7B).

Measurements were collected at 250 μm increments throughout the rostrocaudal extent of the structures of interest (Fig. 7A) by an observer knowledgeable of the treatments. To assess potential bias and inter-observer reliability, a second observer, blind to the treatments, made 10 different measurements in a random subsample of 99 sections. The overall magnitude difference in measurements between the two observers was less than five percent and was not statistically biased among the treatment conditions. Therefore, the "unblind" observer's measurements were used for all graphical and statistical purposes.

Data from the two age groups, PND 18 and PND 25, were pooled. Missing or damaged sections prevented the collection of data from all locations, so statistics were performed on mean values for each animal. Data met the normality assumption for parametric testing ($p > 0.05$, Shapiro-Wilk test as implemented in Prism: GraphPad Software, Inc. La Jolla, CA, USA). Open-side and occluded-side measurements were compared by two-tailed paired t-test. Comparisons of each of these conditions to normal animals were made with unpaired one-tailed t-tests using Welch's correction for unequal variances (Prism). This correction adjusts degrees of freedom based on the variability of a particular sample but the actual number of subjects was invariant across the various measurements. One-tailed tests were justified for comparisons of UNO-treated to normal fossae based on the *a priori* assumption that the morphology of latter group would be intermediate between open and occluded nasal fossae (Coppola, 2012).

One occluded subject from the original eight was excluded from the study because its measurements were two standard deviations away from the other replicates in its group. Measurements on turbinates from the right and left nasal fossae of the four controls were averaged for statistical purposes ($n = 4$).

Computational Methods

An anatomically accurate, three-dimensional model of the right nasal cavity of a 38.8 gram female mouse (CD-1 strain, Charles River Labs) was reconstructed from high-resolution (25 μm isotropic) MRI scans (Fig. 8A & B) following the procedure of Craven et al. (2007). Given the final reconstructed surface model (Fig. 8C), a high-fidelity computational mesh was generated using the hexahedral-dominant, unstructured mesh generation utility, snappyHexMesh, available in the open-source computational continuum mechanics library, OpenFOAM. The mesh (Fig. 8D) contained approximately 19 million computational cells and included a spherical refinement region encompassing the naris to resolve flow entering the nostril, and five wall-normal layers along the internal surfaces of the airway to accurately capture large, near-wall velocity gradients.

A CFD simulation of nasal airflow was carried out assuming steady, laminar flow. Additionally, we assume that the bony internal turbinate structures of the nasal cavity are rigid, and that airway secretions have a negligible influence on the intranasal airflow (see Craven et al. 2009 for further discussion). The computational domain consists of the reconstructed right nasal airway model placed in a large rectangular "box," where far-field atmospheric pressure boundary conditions were specified (as in Craven et al. 2009). No-slip boundary conditions were applied on all solid surfaces of the nasal cavity and a fixed pressure outlet boundary condition was applied at the nasopharynx to induce a physiologically realistic respiratory airflow rate of approximately 36 ml/min based on the mass of the specimen and the allometric relationship provided by Bide et al. (2000) for respiratory minute volume.

The Semi-Implicit Method for Pressure-Linked Equations (SIMPLE) algorithm available in OpenFOAM was used to solve the incompressible continuity and Navier–Stokes equations for steady, laminar flow.

Steady state convergence was achieved when the normalized solution residuals reached 10^{-4}. Additionally, the airflow rate, average shear stress along the airway, and other solution variables were monitored throughout the simulation to ensure convergence of the computed results. The computations were performed on 224 processors of a high-performance parallel computer cluster at Penn State University.

ACKNOWLEDGEMENTS

The authors thank T. Neuberger for the MRI data, and A. Rygg, J. Richter, C. Rumple, A. Ranslow, and A. Quigley for assistance in reconstructing the anatomical model. E.

Weiler suggested this study and provided technical assistance along with G. Lindner and F. Grüllich. J. Seeger, A. Hoffmann and J. Kacza provided equipment and technical advice.

FUNDING

This study was supported by grants from: the National Science Foundation (IOS-1120375 to BAC; IOS-0641433 to DMC), Chenery Endowment, and Rashkind Endowment (DMC)

REFERENCES

Allen, H. (1882). On a revision of the ethmoid bone in the Mammalia, with special reference to the description of this bone and of the sense of smelling in the Cheiroptera. *Bull. Mus. Comp. Zool.* **10**, 135-171.

Bass, S.L., Eser, P., and Daly, R. (2005). The effect of exercise and nutrition on the mechanostat. *J. Musculoskelet. Neuronal Interact*. **5**, 239-254.

Bide, R.W., Armour, S. J. and Yee, E. (2000). Allometric respiration/body mass data for animals to be used for estimates of inhalation toxicity to young adult humans. *Journal of Applied Toxicology*, 20(4):273–290.

Bidwell, J.P. and Pavalko, F. M. (2010). Mechanosomes carry a loaded message. *Science Sig.* **3 (153),** pe51.

Coppola, D. M., Waguespack, A. M., Reems, M. R., Butman, M. L. and Cherry, J. A. (2006). Naris occlusion alters transductory protein immunoreactivity in olfactory epithelium. *Histol. Histopathol.* **21(5)**, 487-501.

Coppola, D. M. (2012). Studies of olfactory system neural plasticity: The contribution of the unilateral naris occlusion technique. *Neural Plasticity*, **vol. 2012**, Article ID 351752, 14 pages. doi:10.1155/2012/351752

Craven, B. A., Neuberger, T., Patterson, E. G., Webb, A. G., Josephson, E. M., Morrison, E. E. and Settles, G. S. (2007). Reconstruction and morphometric analysis of the nasal airway of the dog (*Canis familiaris*) and implications regarding olfactory airflow. *Anat. Rec.* **290**, 1325-1340.

Craven, B. A., Paterson, E.G., Settles, G.S. and Lawson, M.J. (2009). Development and verification of a high-fidelity computational fluid dynamics model of canine nnasal

airflow. *J. Biomech. Eng.*, **131**, 091002.

Davidovich, N.E., Kloog, Y., Wolf, M., and Elad, D. (2011). Mechanophysical stimulation of mucin secretion in cultures of nasal epithelial cells. *Biophys. J.* **100**, 2855-2864.

Ehrlich, P.J. and Lanyon, L.E. (2002). Mechanical strain and bone cell dunction: A review. Ostoeoporsis Int. **13**, 688–700.

Elad, D., Naftali, S., Rosenfeld, M. and Wolf, M. (2006). Physical stresses at the air-wall interface of the human nasal cavity during breathing. *J. Appl. Physiol.* **100**, 1003-1010.

Ginn, J. A., Kumar, M. S. A., McKiernan, B. C. and Powers, B. E. (2008). Nasopharyngeal turbinates in brachycephalic dogs and cats. *J. Am. Anim. Hosp. Assoc.* **44**, 243-249.

Grosmaitre, X., Santarelli, L. C., Tan, J., Luo, M. and Ma, M. (2007). Dual functions of mammalian olfactory sensory neurons as odor detectors and mechanical sensors. *Nat. Neurosci.* **10(3)**, 348–354.

Gudden, B. (1870). Experimentaluntersuchungen über das peripherische und centrale Nervensystem. *Arch. Psychiatr.* **2**, 693-723.

Haradam, S. and Rodan, G. A. (2003). Control of osteoblast function and regulation of bone mass. *Nature* **423**, 349-355.

Huang, H., Kamm, R.D. and Lee, R.T. (2004). Cell mechanics and mechanotransduction: pathways, probes, and physiology. *Am. J. Cell Physiol.* **287**, C1-C11.

Hueber, J. P. (2009). Impulsoszillometrische Untersuchung des intranasalen Atmungswiderstandes vor und nach laserassistierter Turbinektomie zur Therapie des Brachyzephalen Atemnotsyndroms beim Hund. PhD-thesis. Faculty of Veterinary Medicine, University of Leipzig.

Jiang, J., Luo, Y., Dishowitz, M., Wright, A. and Zhao, K. (2010). The first quantititative model of the nasal aerodynamics in mouse. Association for Chemoreception Science Meeting, St Petersburg, FL.

Ku, D.N. (1997). Blood flow in arteries. *Annu. Rev. Fluid Mech.* **29**, 399–434.

Lippert, J. P., Reinhold, P., Smith, H. J., Franco, P., Nather, S. Y., Schlüter, C. and Oechtering, G. U. (2010). Geometry and function of the dog nose: how does function change when form of the nose is changed? *Pneumologie* **64(7)**, 452-453.

Meisami, E. (1976). Effects of olfactory deprivation on postnatal growth of the rat olfactory bulb utilizing a new method for production of neonatal unilateral anosmia. *Brain Res.* **107**, 437-444.

Moore, W. J. (1981). *The Mammalian Skull*. pp. 1-369. Cambridge: Cambridge University Press. 369 p.

Negus, V. (1958). *The Comparative Anatomy and Physiology of the Nose and Paranasal Sinuses*. pp. 1-327. Edinburgh: E. & S. Livingstone.

Rauch, F. (2005). Bone growth in length and width: the Yin and Yang of bone stability. *J. Musculoskelet. Neuronal Interact.* **5(3)**, 194-201.

Rowe, T., Eiting, T. P., Macrini, T. E. and Ketcham, R. A. (2005). Organization of the olfactory and respiratory skeleton in the nose of the gray short-tailed opossum Monodelphis domestica. *J. Mamm. Evol.* **12**, 303–336.

VanValkenburgh, B., Curtis, A., Samuels, J. X., Bird, D., Fulkerson, B., Meachen-Samuels, J. and Slater, G. J. (2011). Aquatic adaptations in the nose of carnivores: evidence from turbinates. *J. Anat.* **218(3)**, 298-310.

Van Valkenburgh, B., Theodor, J., Friscia, A., Pollack, A. and Rowe, T. (2004). Respiratory turbinates of canids and felids: a quantitative comparison. *J. Zool., Lond.* **264**, 281-293.

Wallman, J. and Winawer, J. (2004). Homeostasis of eye growth and the question of myopia. *Neuron* **43**, 447-468.

Walter, A. (2010). Histologische Untersuchung der Nasenmuscheln brachyzephaler und normozephaler Hunde. PhD-thesis. Faculty of Veterinary Medicine, University of Leipzig.

Waguespack, A. M., Reems, M. R., Butman, M. L., Cherry, J. A. and Coppola, D. M. (2005). Naris occlusion alters olfactory marker protein immunoreactivity in olfactory epithelium. *Brain Res.* **1044(1)**, 1-7.

Wu, K. N., Tan, B. K, Howard, J. D., Conley, D. B. and Gottfried, J. A. (2012). Olfactory input is critical for sustaining odor quality codes in human orbitofrontal cortex. *Nat. Neurosci.* **5(9)**, 313-319.

FIGURE LEGENDS

Figure 1. A. Normal coronal H & E-stained section through nasal cavity showing the nasoturbinate (Nt) and maxilloturbinate (Mt). OE = olfactory epithelium; S = nasal septum. Note the remarkable symmetry of the turbinates in the two nasal fossae. **B.** Similar section as **A** from a UNO animal. X = occluded fossa. Note "filigree" morphology of Nt from occluded fossa. Scale bar for **A** & **B** = 300µm **C.** Olfactory Marker Protein (OMP) immunolabeling of Nt from open fossa of UNO mouse. **D.** Same animal and label as in **C** but from occluded fossa. . The denser OMP labeling on the occluded side, obvious in these photomicrographs, has been previously reported (Waguespack et al., 2005; Coppola et al., 2006). Scale bar for **C** & **D** = 120 µm. **E.** (below). Drawings of coronal sections from Nt at approximately 250 µm intervals throughout their rostrocaudal extent. Turbinates from the non-occluded (top) and occluded fossa (bottom) of one mouse are illustrated. Rostral-most section is to the left. Dorsal is toward top. RE = respiratory epithelium.

Figure 2. Area and perimeter measurements of cross-sections of Nt at different rostrocaudal positions for two UNO animals (**A**, **C**) and two normal controls (**B**, **D**). **E.** Mean (± s.e.m.) area/perimeter (A/P) group data pooled across rostrocaudal location for occluded and open fossae (mean, n = 7) as well as normal fossae (n = 4). Means for open and occluded fossae were compared by paired t-test. Other comparisons were by unpaired t-test. Perimeter values alone were not significantly different among the groups.

Figure 3. Length and width measurements of two unilaterally naris-occluded animals (**A, C**) and two controls (**B, D**). **E.** Mean (± s.e.m.**)** group data of length-width ratio. Means for open and occluded fossae were compared by paired t-test. Other comparisons were by unpaired t-test. Note: occluded-side Nts are somewhat longer and much wider than open-side Nts resulting in a filigree appearance. Normal control subjects are intermediate, though not significantly so.

Figure 4. Width of dorsal meatus taken at inflection point for two UNO animals (**A, C**) and two normal controls (**B, D**). **E**. Mean (± s.e.m.**)** group data for width of dorsal meatus. Means for open and occluded fossae were compared by paired t-test. Other comparisons were by unpaired

t-test. Note: occluded-side fossae are wider than open-side fossae but both are wider than controls.

Figure 5. Distance (offset) from medial-most border of NT and the ethmoturbinates to closest point of nasal septum. **A.** Data from one UNO subject showing turbinates II through IV on occluded side are shifted laterally compared to open side. **B.** Data from one control mouse showing high degree of symmetry in turbinate offset. **C.** Mean (± s.e.m.**)** of group data pooled across rostrocaudal samples. Columns with different lowercase letters are significantly different by paired or un-paired t-test ($p < 0.05$). N = Normal controls; O = open (non-occluded fossa); X = closed (occluded fossa).

Figure 6. Distribution of shear stress magnitude in the nasal airway of the mouse from CFD simulations of respiratory airflow in the nose. Contours of shear stress magnitude are shown on transverse cross-sections of the airway wall in the respiratory (1-4) and olfactory (5,6) regions. NT: nasoturbinate; MT: maxilloturbinate.

Figure 7. A. Drawing of midsagittal view of mouse with septum removed. Arrows mark approximate rostrocaudal limits of histological samples. Nt (red) = nasoturbinate; Mt (green) = maxilloturbinate; roman numerals (blue) label ethmoturbinates; Np = nasopharynx; Ob = olfactory bulb; Dotted line marks approximate location from which coronal section in **B** was taken. **B.** Coronal section from normal (control) mouse stained with H & E illustrating morphometric measurements (dashed lines on right; see methods). **a** = width of dorsal meatus; **b** = length of turbinate; **c** = width of turbinate; **d** = turbinate-septum offset; **e** = perimeter of turbinate; **oe** = olfactory epithelium; **DM** = dorsal meatus; **tb** = turbinate bone; **re** = respiratory epithelium; **Nt** = nasoturbinate; **S** = nasal septum; **Mt** = maxilloturbinate; **VM** = ventral meatus; scale bar = 300 µm.

Figure 8. Anatomically accurate computational model of the mouse nasal cavity. High-resolution MRI scans (**A, B**) were acquired in a cadaver specimen and were used to reconstruct a three-dimensional surface model of the right nasal airway (**C**). A high-

fidelity computational mesh of the nasal airway (**D**) was generated from the anatomical reconstruction and used in computational fluid dynamics (CFD) simulations of nasal airflow.

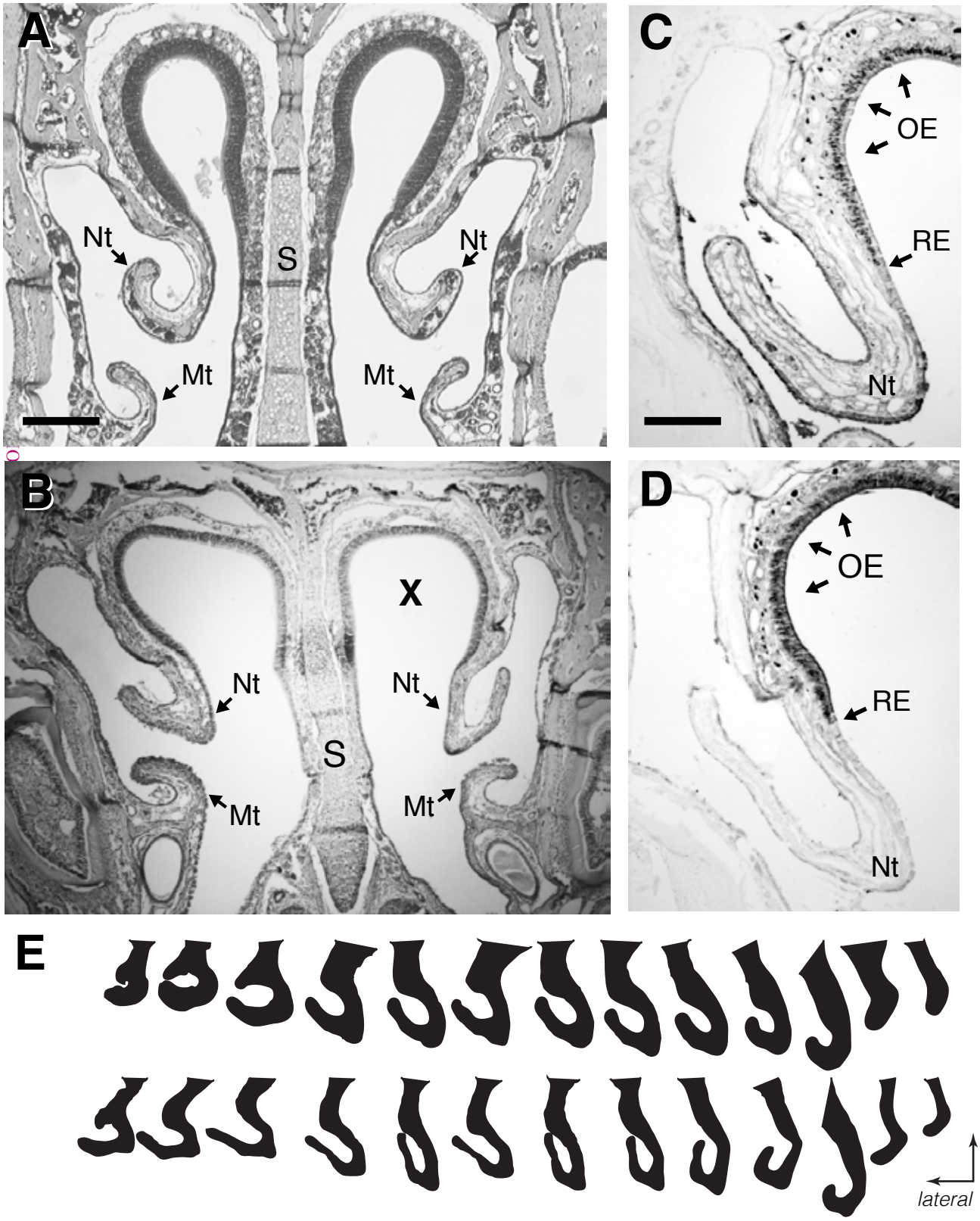
A
Nt
S
Nt
Mt
Mt
C
OE
RE
Nt
B
X
Nt
Nt
S
Mt
Mt
D
OE
RE
Nt
E
dorsal
lateral

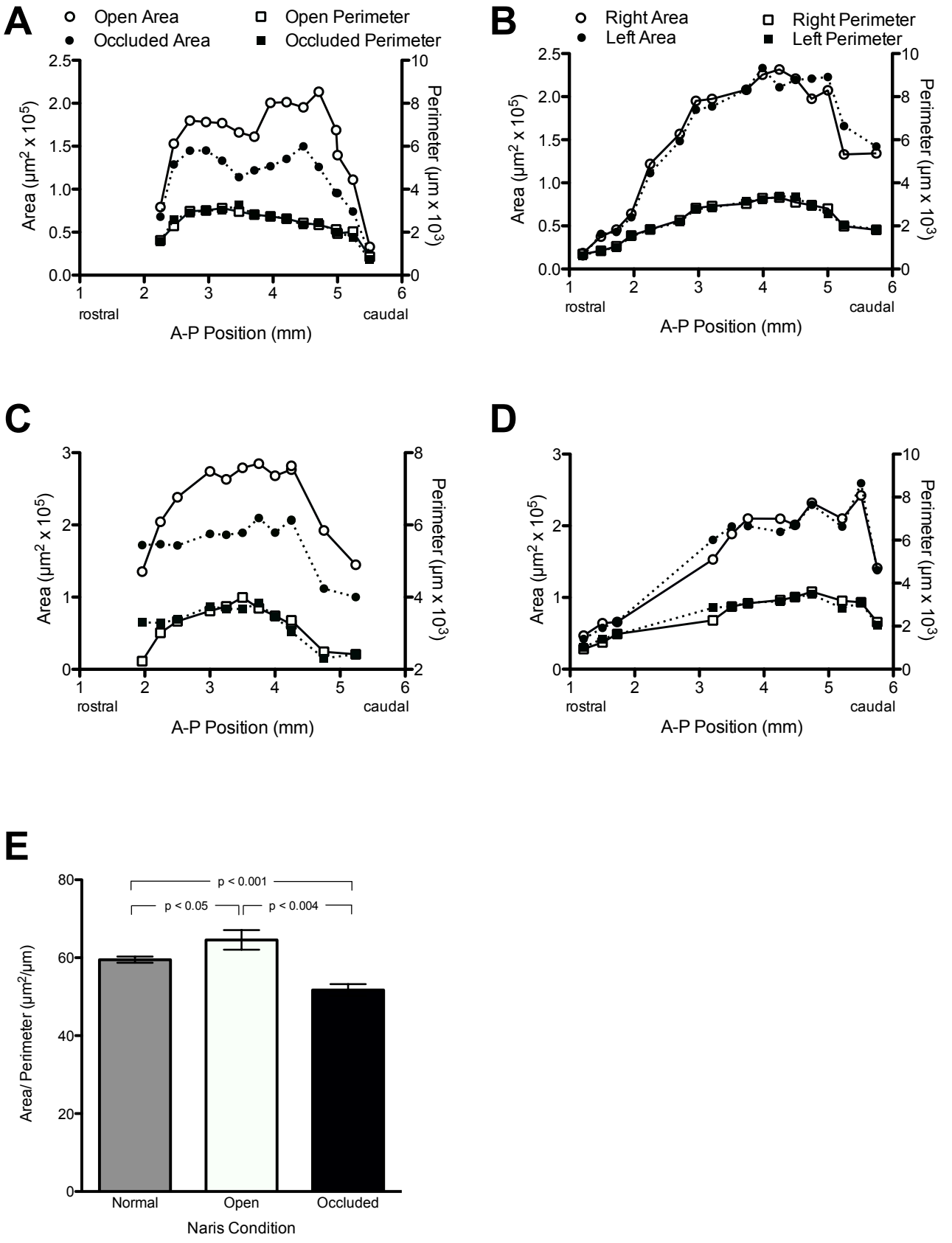
A
Open Area
Occluded Area
Open Perimeter
Occluded Perimeter
Area (μm² x 10⁵)
Perimeter (μm x 10³)
rostral
caudal
A-P Position (mm)
B
Right Area
Left Area
Right Perimeter
Left Perimeter
Area (μm² x 10⁵)
Perimeter (μm x 10³)
rostral
caudal
A-P Position (mm)
C
Area (μm² x 10⁵)
Perimeter (μm x 10³)
rostral
caudal
A-P Position (mm)
D
Area (μm² x 10⁵)
Perimeter (μm x 10³)
rostral
caudal
A-P Position (mm)
E
p < 0.001
p < 0.05
p < 0.004
Area/ Perimeter (μm²/μm)
Normal
Open
Occluded
Naris Condition

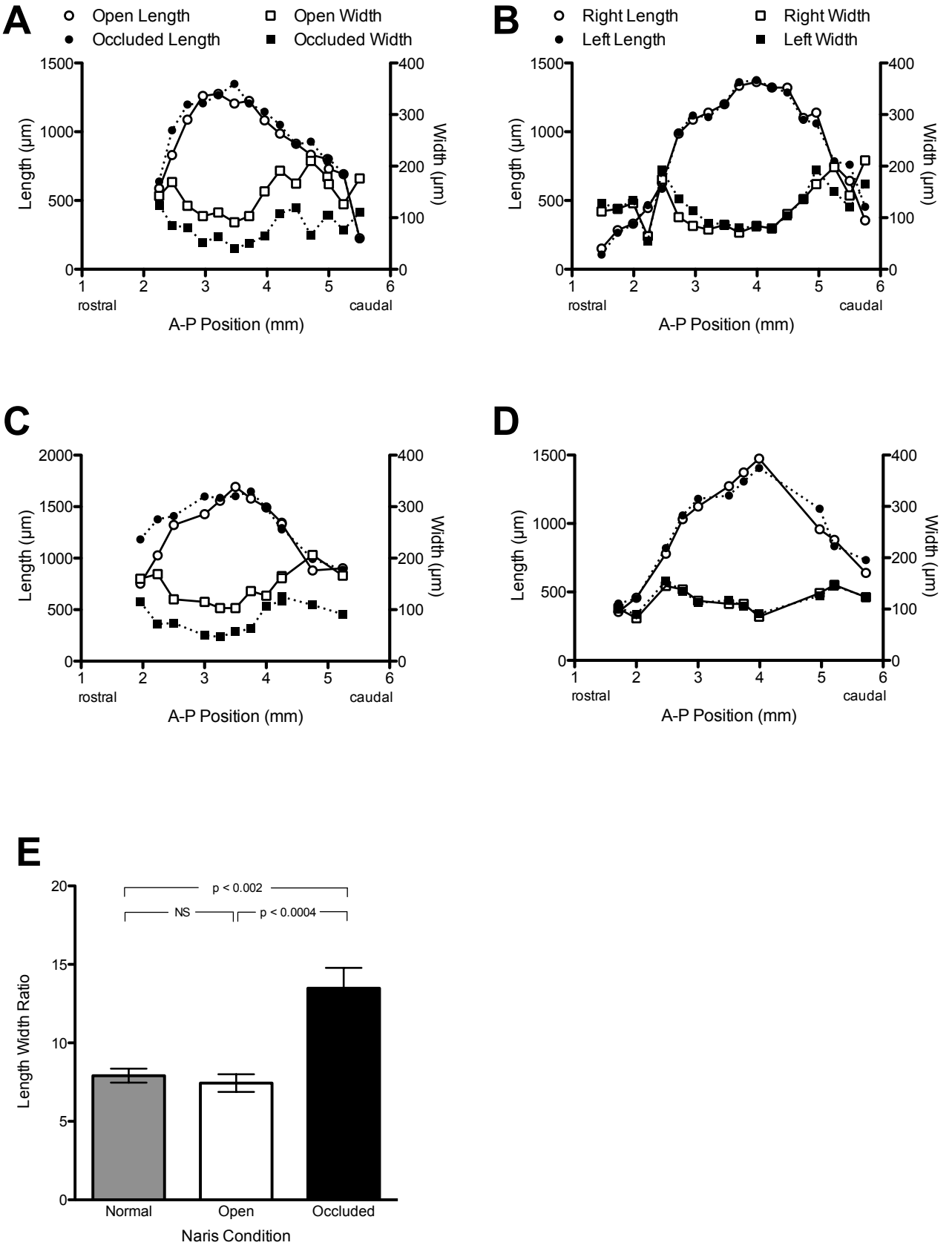
A
Open Length
Occluded Length
Open Width
Occluded Width
Length (µm)
Width (µm)
rostral
caudal
A-P Position (mm)
B
Right Length
Left Length
Right Width
Left Width
C
D
E
p < 0.002
NS
p < 0.0004
Length Width Ratio
Normal
Open
Occluded
Naris Condition

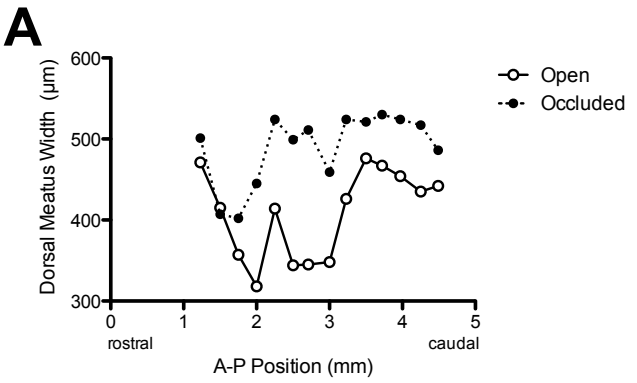
A
Dorsal Meatus Width (µm)
600
500
400
300
Open
Occluded
0
1
2
3
4
5
rostral
caudal
A-P Position (mm)

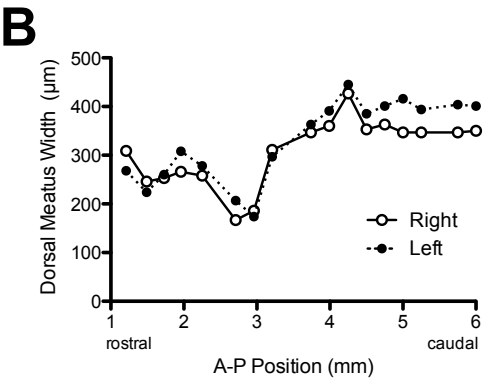
B
Dorsal Meatus Width (µm)
500
400
300
200
100
0
Right
Left
1
2
3
4
5
6
rostral
caudal
A-P Position (mm)

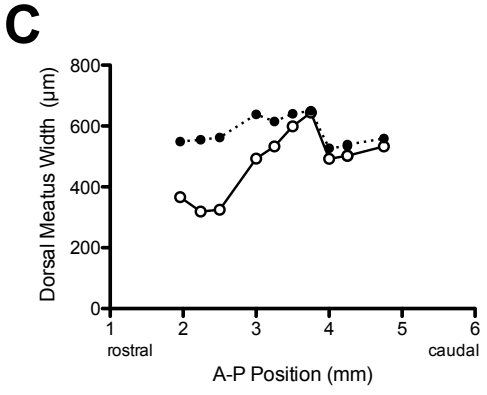
C
Dorsal Meatus Width (µm)
800
600
400
200
0
1
2
3
4
5
6
rostral
caudal
A-P Position (mm)

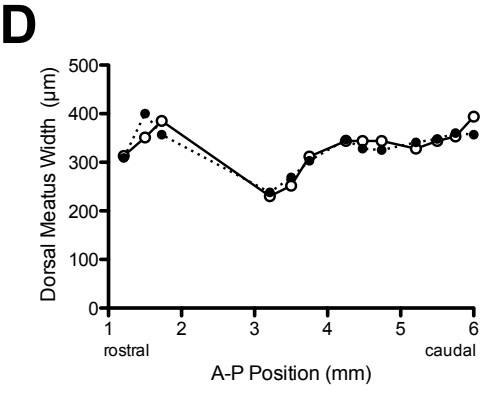
D
Dorsal Meatus Width (µm)
500
400
300
200
100
0
1
2
3
4
5
6
rostral
caudal
A-P Position (mm)

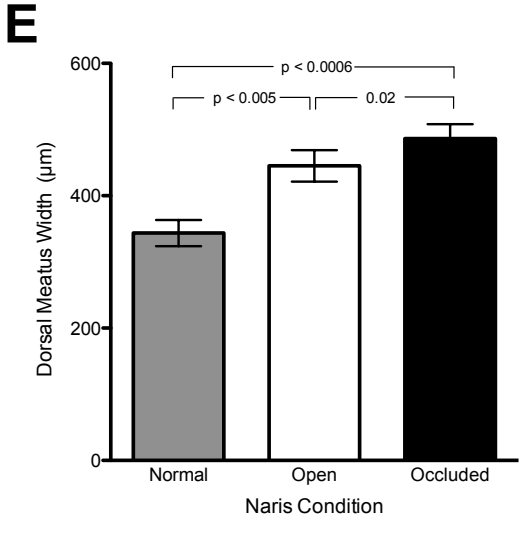
E
Dorsal Meatus Width (µm)
600
400
200
0
p < 0.0006
p < 0.005
0.02
Normal
Open
Occluded
Naris Condition

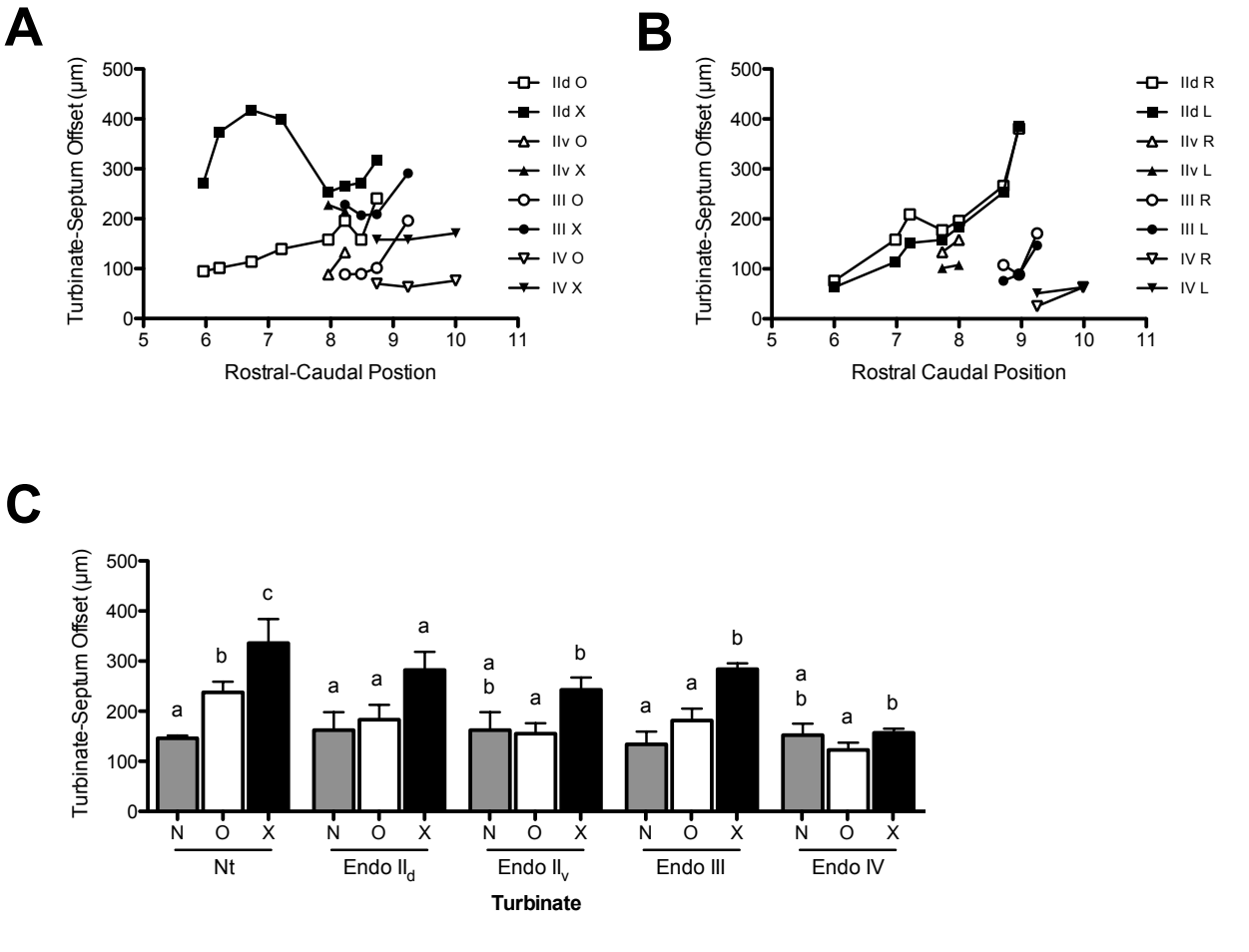
A
Turbinate-Septum Offset (µm)
500
400
300
200
100
0
5
6
7
8
9
10
11
Rostral-Caudal Postion
IId O
IId X
IIv O
IIv X
III O
III X
IV O
IV X
B
Turbinate-Septum Offset (µm)
Rostral Caudal Position
IId R
IId L
IIv R
IIv L
III R
III L
IV R
IV L
C
Turbinate-Septum Offset (µm)
a
b
c
a
a
a
a
b
a
b
a
a
b
a
b
a
b
a
b
N
O
X
Nt
Endo II$_d$
Endo II$_v$
Endo III
Endo IV
Turbinate

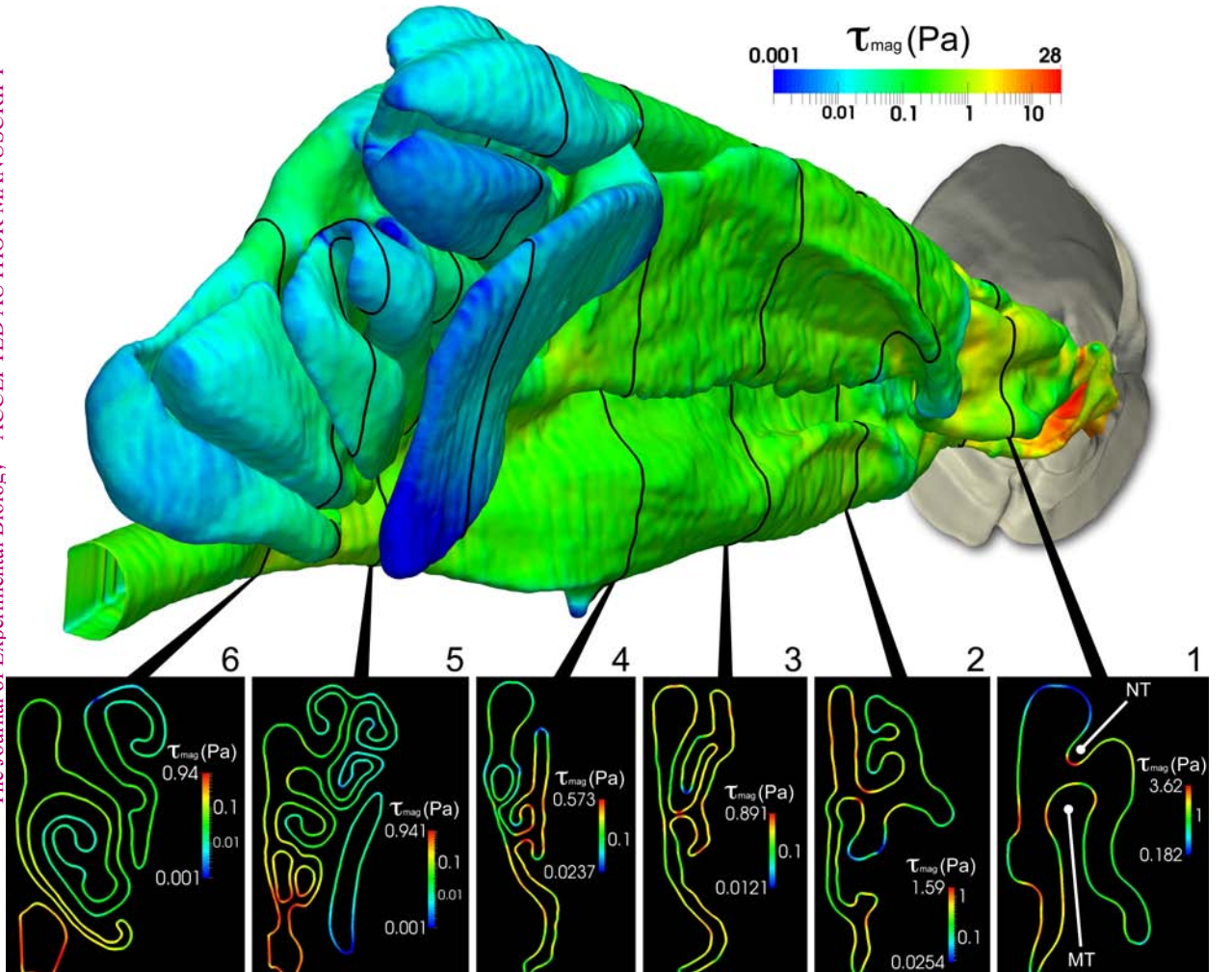

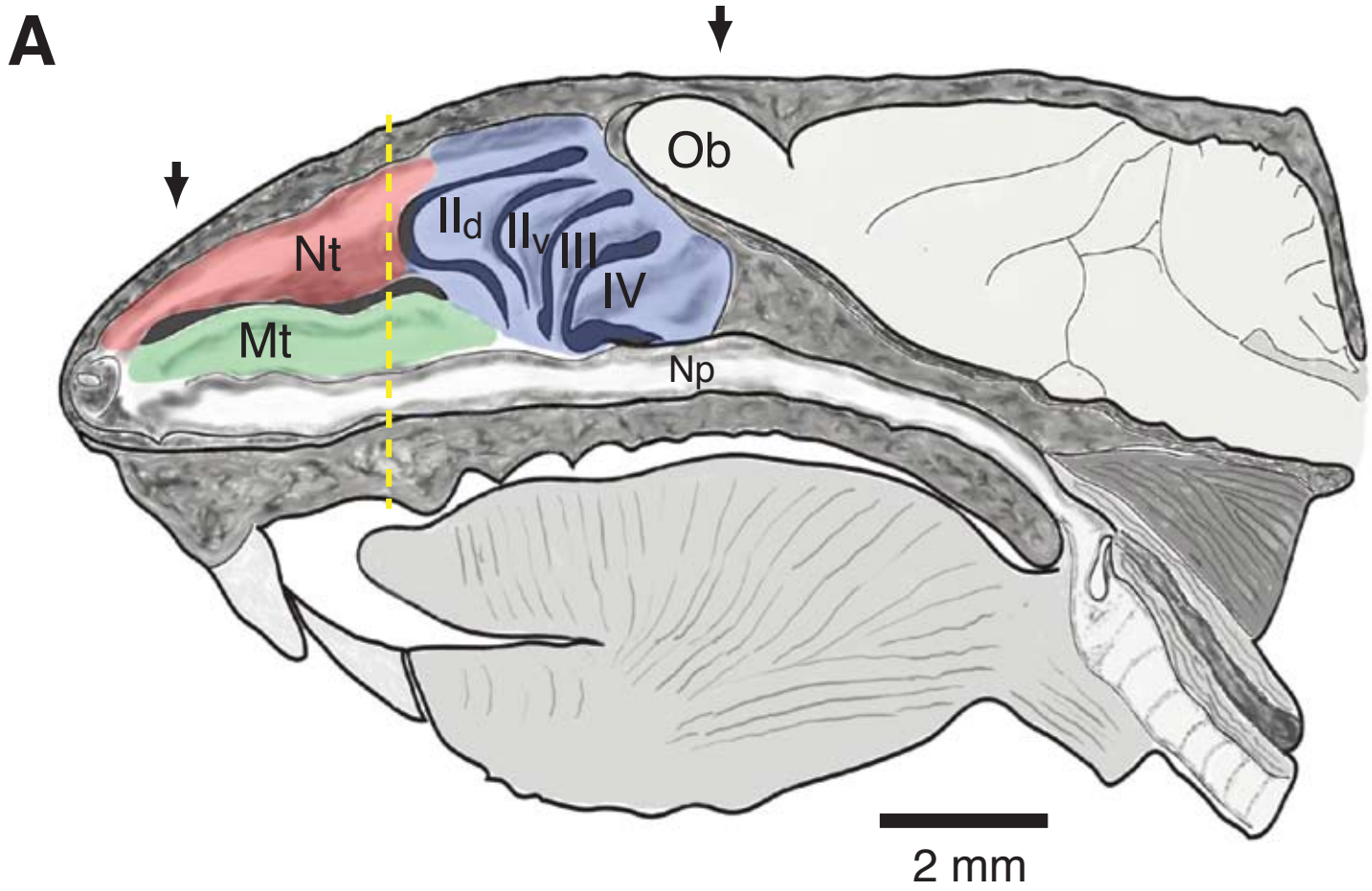

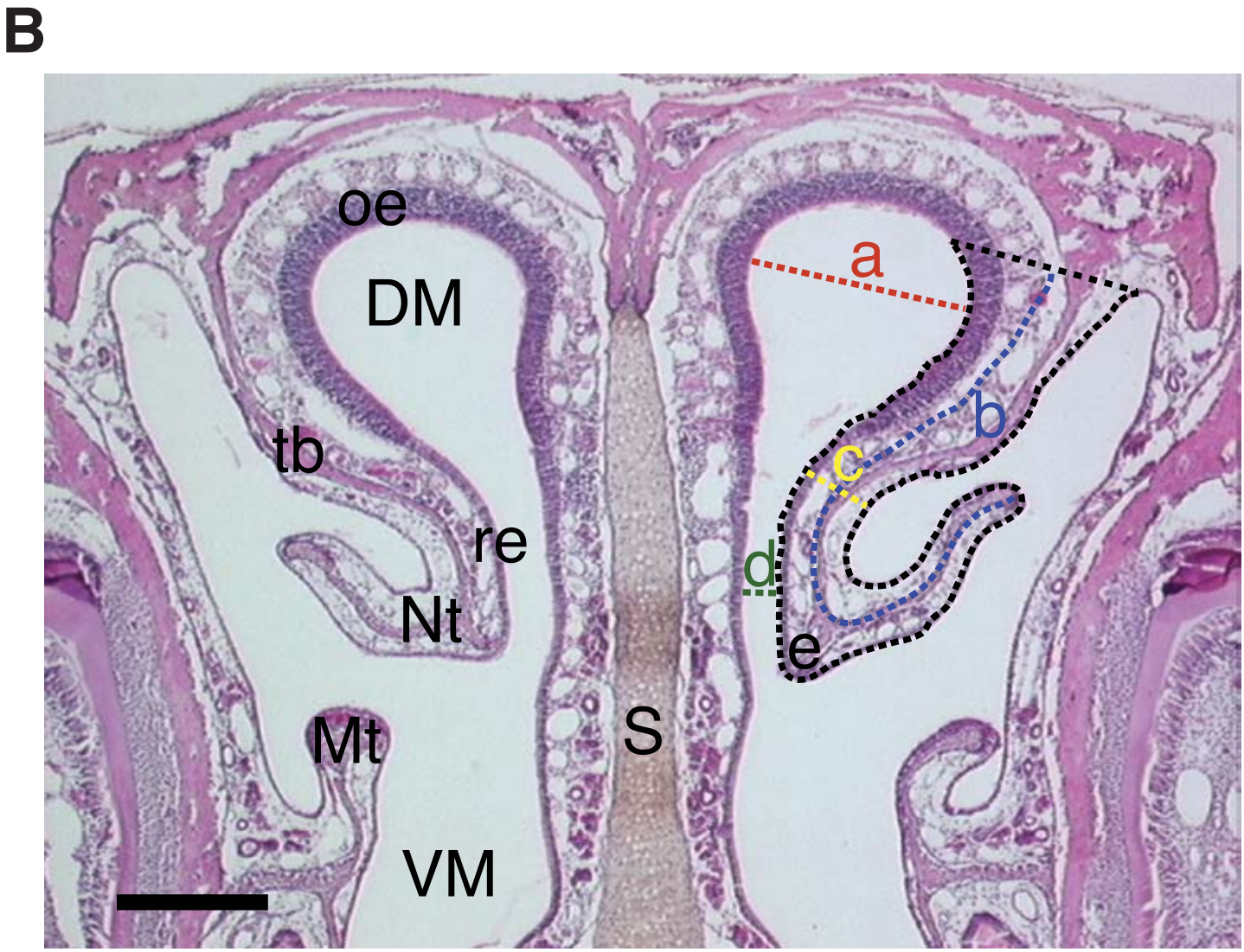

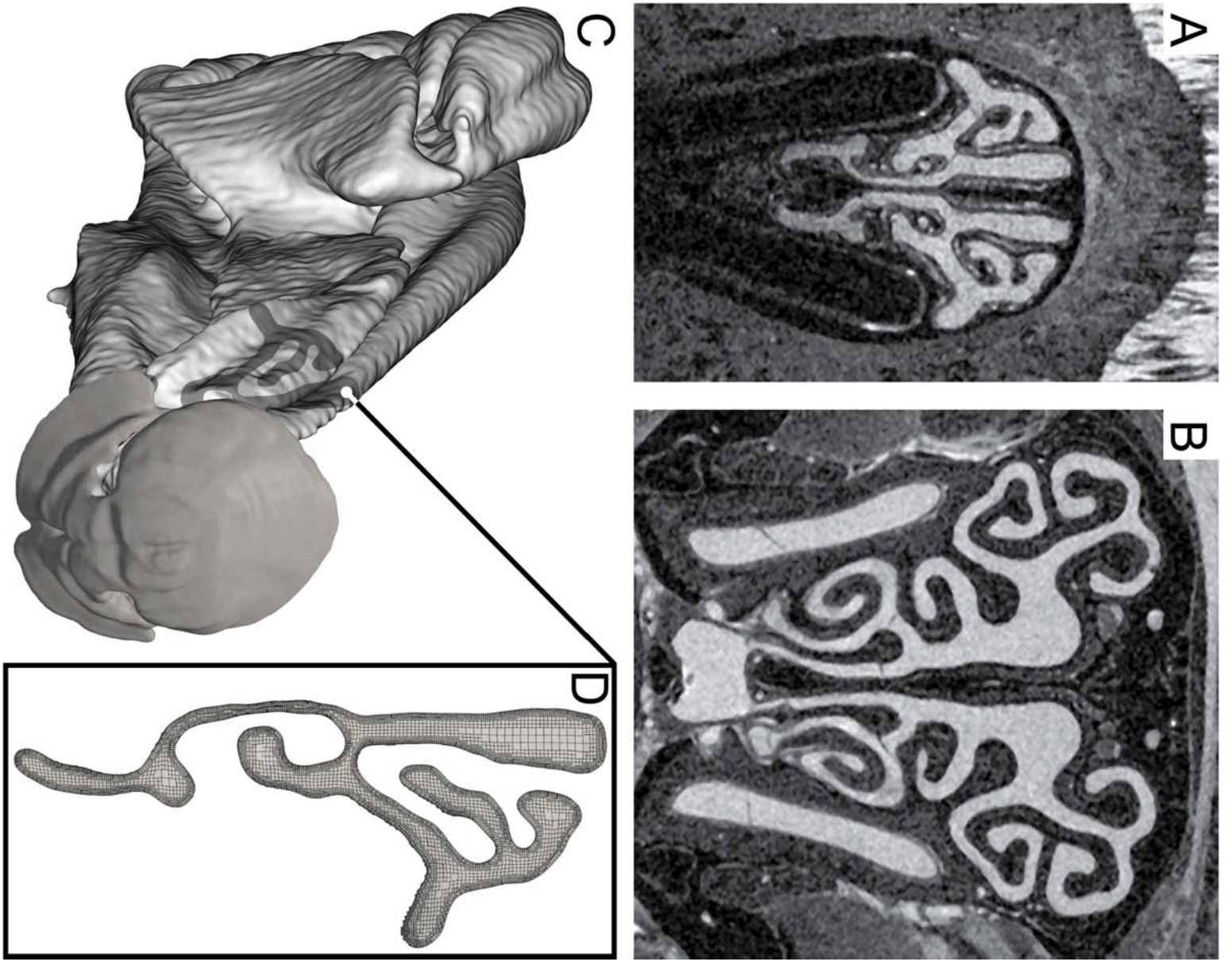
A
B
C
D